# High-fidelity Aerostructural Optimization Benchmark for Aircraft Propellers in Hover

Seth A. Zoppelt\*, Heyecan U. Koyuncuoglu<sup>†</sup>, Ping He<sup>‡</sup>, Iowa State University, Ames, Iowa, 50011, USA

This paper proposes an aerostructural optimization benchmark for aircraft propellers working in a hover condition. This benchmark uses an untwisted and untapered blade with a NACA0012 sectional profile as the baseline design. The objective function is the propeller shaft power coefficient. The design variables include the propeller twist, shape, chord, span, and rotation speed. The constraints include the propeller thrust coefficient, mass, von Mises stress, and geometry (e.g., thickness and curvature). We propose three different optimization configurations with various combinations of design variables. The proposed propeller aerostructural optimization benchmark can be solved using various optimization algorithms and modeling fidelities. This paper showcases a high-fidelity gradient-based optimization approach. To be more specific, we use the finite-volume computational fluid dynamics and finite-element structural dynamics solvers to simulate the fluid and solid domains, respectively. We then use the discrete adjoint approach to compute the derivatives for gradientbased optimization with a large number of design variables. To consider fluid-structure interaction and coupled derivative computation, we utilize OpenMDAO/MPhys, an open-source framework that facilitates high-fidelity multidisciplinary design optimization. We compare the objective, constraints, and distributions of spanwise shape, twist, and thrust between the baseline and optimized designs. This study has the potential to build a common benchmark and promote collaboration in the propeller multidisciplinary design optimization community.

# I. Introduction

Propeller aircraft have received increasing interest in recent years because they are widely used for unmanned aerial vehicles (UAVs) and urban air mobility (UAM) vehicles. The propeller aerodynamic performance directly impacts the aircraft's energy consumption and flight range. Multidisciplinary design optimization (MDO) [1, 2] is a promising technique for maximizing propeller performance. It uses multiphysics computer simulations to find the best possible design automatically and has the potential to significantly reduce the design period. To allow large design freedom, we need a large number of design variables to parameterize the complex propeller blade geometry. Therefore, a gradient-based optimization algorithm coupled with the adjoint gradient computation approach [3–6] forms a powerful combination. The gradient-based optimization approach has been widely used for optimizing various aerospace engineering problems, including aircraft [7–10], wind turbine [11, 12], and gas turbines [13–16]. It has also been used in propeller designs; however, existing gradient-based propeller designs typically use low-fidelity models [17, 18], e.g., blade element momentum (BEM). High-fidelity MDO for aircraft propellers has not been well studied.

In this study, we propose an aerostructural optimization benchmark for aircraft propellers. This benchmark uses an untwisted and untapered blade with a NACA0012 sectional profile as the baseline design. The objective function is the propeller shaft power coefficient. The design variables include the propeller shape, span, twist, chord, and rotation speed. The constraints include the propeller thrust coefficient, mass, von Mises stress, and geometry (e.g., thickness and curvature). The propeller is working in a hover condition. We solve the aerostructural optimization problem using high-fidelity gradient-based optimization based on the OpenMDAO/MPhys framework. OpenMDAO [19] is an open-source multidisciplinary design, analysis, and optimization framework developed by NASA. OpenMDAO has been widely used for large-scale design optimization in aerospace engineering applications. MPhys [20] is a recently developed derivative of OpenMDAO. MPhys facilitates the coupling of high-fidelity solvers with various disciplines. We have recently coupled our open-source discrete adjoint solver called DAFoam [21–23] into the OpenMDAO/MPhys

<sup>\*</sup>PhD Student, Department of Aerospace Engineering, AIAA Student Member.

<sup>†</sup>PhD Student, Department of Aerospace Engineering, AIAA Student Member.

<sup>‡</sup> Assistant Professor, Department of Aerospace Engineering, AIAA Senior Member. Email: phe@iastate.edu

framework for aerostructural optimization [24, 25]. The aerodynamic and structural analysis will be conducted by using computational fluid dynamics (CFD) and finite-element method (FEM) solvers, respectively.

The rest of this paper is organized as follows. In Section II, we elaborate on the aerostructural analysis and optimization framework, followed by the detailed optimization results in Section III. Finally, in Section IV, conclusions are drawn and perspectives and future improvements are provided.

# II. Method

In this section, we elaborate on the mathematical background of our aerostructural analysis and optimization framework.

## A. Aerodynamic Analysis using CFD

We use OpenFOAM's rhoSimpleFoam solver [26] to simulate the flow over propeller blades. It solves 3D, steady-state turbulent flows governed by the compressible Navier-Stokes (NS) equations written in the multiple-reference-frame (MRF) format.

$$\nabla \cdot (\rho U_a) = 0, \tag{1}$$

$$\nabla \cdot (\rho U_r U_a) + \omega \times U_a + \nabla p - \nabla \cdot \mu_{\text{eff}} (\nabla U_a + \nabla U_a^T) = 0, \tag{2}$$

$$\nabla \cdot (\rho e U_a) + \nabla \cdot (0.5\rho |U|_a^2 U_a + \rho U_a) - \alpha_{\text{eff}} \nabla \cdot (\nabla e) = 0, \tag{3}$$

where  $U_a$  and  $U_r$  are the absolute and relative velocities, respectively, and they are related through  $U_a = U_r + \omega \times x_c$  with  $\omega$  being the rotational speed vector and  $x_c$  being the cell-center coordinate vector. The above governing equations are solved using the compressible form of the SIMPLE algorithm based on the absolute velocity in the stationary frame; however, the flux for the convective term in the momentum equation (2) is computed using the relative velocity in the rotating frame.

The Spalart-Allmaras model is used to connect the turbulent eddy viscosity to the mean flow variables, the details of this formulation and description of the terms can be found in their paper [27]:

$$\nabla \cdot (U_a \widetilde{v}) + \frac{1}{\sigma} \left\{ \nabla \cdot \left[ (v + \widetilde{v}) \nabla \widetilde{v} \right] + C_{b1} |\nabla \widetilde{v}|^2 \right\} - C_{b1} \widetilde{S} \widetilde{v} + C_{w1} f_w \left( \frac{\widetilde{v}}{d} \right)^2 = 0$$
 (4)

# **B. Structural Analysis using FEM**

We use TACS [28], an open-source finite-element solver, to simulate the propeller blade structure. TACS has linear and geometrically nonlinear simulation capabilities; however, only linear analysis is used in this paper. The linear elastic governing equation is as follows:

$$Ku - F = 0 ag{5}$$

where K is the structural stiffness matrix, u is the structural displacement vector, and F is the load vector. Note that only the aerodynamic pressure load is included in the load vector, and the centrifugal force is not included.

#### C. Aerostructural Analysis with Coupled CFD and FEM

The aerostructural coupling is implemented in the OpenMDAO/MPhys framework. As mentioned above, Open-MDAO [19] is an open-source multidisciplinary design, analysis, and optimization framework developed by NASA. MPhys [20] is a recently developed derivative of OpenMDAO with a flexible interface that allows the multidisciplinary coupling of various high-fidelity solvers, such as finite-volume computational fluid dynamics and finite-element computational structural dynamics.

Figure 1 shows the aerostructural analysis using the OpenFOAM and TACS solvers. The inputs are the latest design surface geometry (i.e., propeller blade geometry) in the optimization loop, baseline CFD and FEM meshes, and CFD and FEM design variables (e.g., blade rotation speed). The outputs are the converged aerostructural state variables (e.g., velocity, pressure, and structural displacement) and objective and constraint functions (e.g., propeller power and thrust).

The "Aerostructural analysis" (main driver) starts by computing the "Updated CFD surface mesh" based on the "Design surface" geometry and the "CFD surface mesh displacement" computed from the "Displacement transfer"

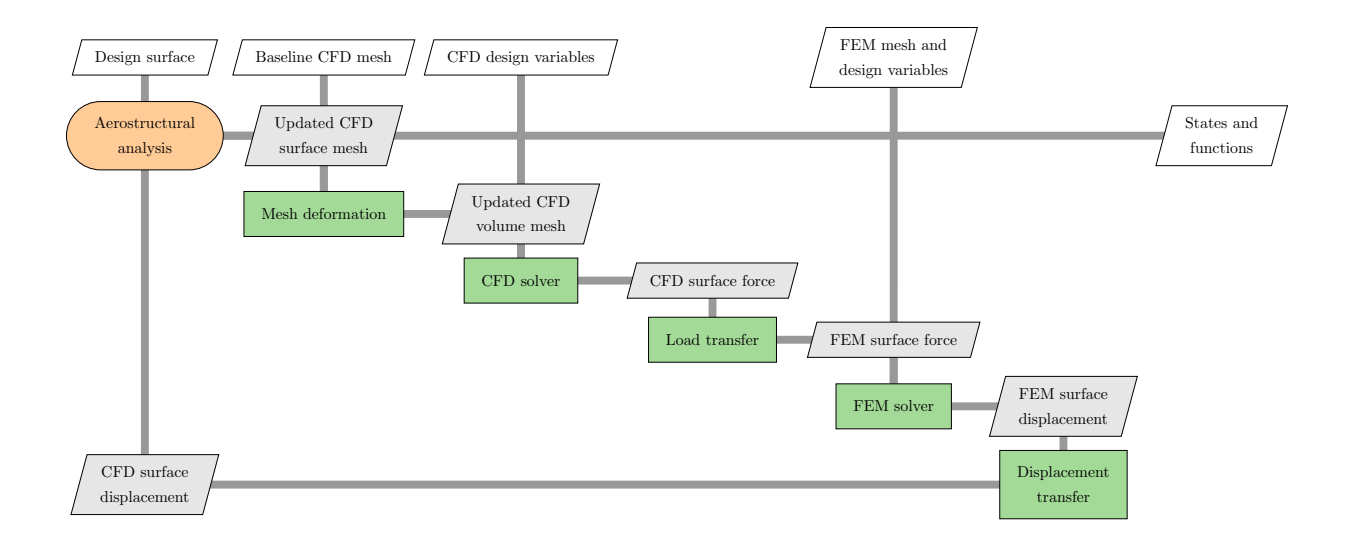


Fig. 1 Schematic of aerostructural analysis using OpenMDAO/MPhys [20]. Here we use the XDSM representation. The diagonal blocks are the components, and the off-diagonal blocks are data transfers. The CFD and FEM solvers are OpenFOAM and TACS, respectively.

component (in the first iteration, the displacement will be zero). Then, the "Mesh deformation" component will use the "Updated CFD surface mesh" to compute the "Updated CFD volume mesh". Next, the "CFD solver" component receives the "Updated CFD volume mesh", simulates the flow fields, extracts the "CFD surface force", and passes it to the "Load transfer" component. The "Load transfer" component will interpolate the "CFD surface force" to the "FEM surface force" and pass the force to the "FEM solver". Then, the "FEM solver" component will compute the structural displacement and extract the "FEM surface displacement" and pass it to the "Displacement transfer" component. The "Displacement transfer" component will then interpolate the "FEM surface displacement" to the "CFD surface displacement", and then pass it to the "Aerostructural analysis" main driver to start the next iteration. The above process will repeat until the residuals for both the CFD and FEM solvers are small than the prescribed tolerances.

MPhys provides a general aerostructural template called "Scenario" to facilitate the above coupling between CFD and FEM solvers. MPhys currently supports solvers such as ADflow [29], FUN3D [30, 31], OpenAeroStruct [32], and TACS. We have developed a Python interface called mphys\_dafoam to extend the aerostructural scenario so it can use OpenFOAM and DAFoam as the CFD and adjoint solvers (the adjoint will be elaborated on in the next section). The mesh deformation component uses IDWarp [33], an open-source inverse distance weighted mesh deformation code. The load and displacement transfer components are based on the Meld approach from a generic aeroelastic analysis and adjoint-based gradient evaluation tool called FUNtoFEM [34]. TACS is used as the FEM solver. The CFD and FEM iteration is conducted using the nonlinear block Gauss—Seidel solver in OpenMDAO with an Aitken relaxation approach.

#### D. Discrete Adjoint Computation

We use the discrete adjoint method to compute the derivatives for optimization. The function of interest is the function of both the design and the state variables:

$$f = f(\mathbf{x}, \mathbf{w}) \tag{6}$$

where  $x \in \mathbb{R}^{n_x}$  is the design vector, and  $w^n \in \mathbb{R}^{n_w}$  is the flow state variable vector.  $n_x$  and  $n_w$  are the numbers of design and state variables, respectively. The chain rule is applied to compute df/dx:

$$\left[\frac{\mathrm{d}f}{\mathrm{d}x}\right]_{1\times n_x} = \left[\frac{\partial f}{\partial x}\right]_{1\times n_x} + \left[\frac{\partial f}{\partial w}\right]_{1\times n_w} \left[\frac{\mathrm{d}w}{\mathrm{d}x}\right]_{n_w\times n_x}$$
(7)

The partial derivatives in Eq. (7) are relatively cheap to evaluate because they only involve explicit computations. However, the total derivative  $d\mathbf{w}/d\mathbf{x}$  is expensive because both terms are determined implicitly.

Similarly, the chain rule is applied to the flow residual vector,  $\mathbf{R} \in \mathbb{R}^{n_w}$ , to solve the  $d\mathbf{w}/d\mathbf{x}$  term. Because the governing equations have to be satisfied regardless of the values of design variables x, the total derivative  $d\mathbf{R}/d\mathbf{x}$  must be zero:

$$\frac{\mathrm{d}\mathbf{R}}{\mathrm{d}\mathbf{x}} = \frac{\partial \mathbf{R}}{\partial \mathbf{x}} + \frac{\partial \mathbf{R}}{\partial \mathbf{w}} \frac{\mathrm{d}\mathbf{w}}{\mathrm{d}\mathbf{x}} = 0 \tag{8}$$

Substituting Eq. (8) into Eq. (7):

$$\left[\frac{\mathrm{d}f}{\mathrm{d}x}\right]_{1\times n_{x}} = \left[\frac{\partial f}{\partial x}\right]_{1\times n_{x}} - \left[\frac{\partial f}{\partial w}\right]_{1\times n_{w}} \left[\frac{\partial R}{\partial w}\right]_{n_{w}\times n_{w}}^{-1} \left[\frac{\mathrm{d}R}{\mathrm{d}x}\right]_{n_{w}\times n_{x}} = \left[\frac{\partial f}{\partial x}\right]_{1\times n_{x}} - \left[\psi^{T}\right]_{1\times n_{w}} \left[\frac{\mathrm{d}R}{\mathrm{d}x}\right]_{n_{w}\times n_{x}} \tag{9}$$

where  $\psi$  is the adjoint vector. Transposing the Jacobian and solving with  $[df/dw]^T$  as the right-hand side yields the adjoint equations:

$$\left[\frac{\partial \mathbf{R}}{\partial \mathbf{w}}\right]_{n_w \times n_w}^T \cdot \left[\mathbf{\psi}\right]_{n_w \times 1} = \left[\frac{\partial f}{\partial \mathbf{w}}\right]_{n_w \times 1}^T \tag{10}$$

Substituting Eq. (10) into Eq. (7), we can compute the total derivatives:

$$\frac{\mathrm{d}f}{\mathrm{d}x} = \frac{\partial f}{\partial x} - \psi^T \frac{\partial \mathbf{R}}{\partial x} \tag{11}$$

Since the design variable is not explicitly present in Eq. (11), the adjoint equations are needed to solve only once for each function of interest. Therefore, its computational cost is independent of the number of design variables but proportional to the number of objective functions. This approach is also known as the adjoint method, and it is advantageous for aerodynamic design. Because typically, there are only a few functions of interest, but several hundred design variables can be used.

## E. Aerostructural Adjoint Coupling

The above adjoint formulation assumes the CFD and FEM state variables are combined into one and solved in a coupled manner. However, this will increase the size of the Jacobian matrix and the corresponding memory cost. We use a segregated method (block Gauss-Seidel) to solve the coupled aerostructural adjoint, as shown below.

$$\begin{bmatrix} \frac{\partial \mathbf{R}_{\text{CFD}}}{\partial \mathbf{w}_{\text{CFD}}}^T & \frac{\partial \mathbf{R}_{\text{FEM}}}{\partial \mathbf{w}_{\text{CFD}}}^T \\ \frac{\partial \mathbf{R}_{\text{CFD}}}{\partial \mathbf{w}_{\text{FEM}}}^T & \frac{\partial \mathbf{R}_{\text{FEM}}}{\partial \mathbf{w}_{\text{FEM}}}^T \end{bmatrix} \begin{bmatrix} \mathbf{\Psi}_{\text{CFD}} \\ \mathbf{\Psi}_{\text{FEM}} \end{bmatrix} = \begin{bmatrix} \frac{\partial f}{\partial \mathbf{w}_{\text{CFD}}}^T \\ \frac{\partial f}{\partial \mathbf{w}_{\text{FEM}}}^T \end{bmatrix}$$
(12)

where the subscript CFD and FEM denote the residual and state variables for the CFD and FEM solvers, respectively. We use DAFoam [22, 35] to solve the CFD adjoint equation:

$$\frac{\partial \mathbf{R}_{\text{CFD}}}{\partial \mathbf{w}_{\text{CFD}}}^T \mathbf{\Psi}_{\text{CFD}} = \frac{\partial f}{\partial \mathbf{w}_{\text{CFD}}}^T \tag{13}$$

DAFoam is an open-source discrete adjoint implementation for OpenFOAM. DAFoam uses a Jacobian-free adjoint approach, in which the partial derivatives and matrix-vector products are computed using the automatic differentiation method, as detailed in Kenway et al. [6]. DAFoam uses the generalized minimal residual (GMRES), an iterative linear equation solver in the PETSc [36] library to solve the adjoint equation. A nested preconditioning strategy with the additive Schwartz method is used as the global preconditioner and the incomplete lower and upper (ILU) factorization approach with one level of fill-in for the local preconditioning. The preconditioner matrix  $[\partial R/\partial w]_{RC}^T$  is constructed by approximating the residuals and their linearizations [21] to improve convergence. The construction of  $[\partial R/\partial w]_{RC}^T$  is only done for the first time instance and then is reused for the adjoint equation. This treatment significantly reduces the adjoint runtime because the constructing  $[\partial R/\partial w]_{RC}^T$  consists of about 30% of the adjoint runtime.

We use TACS to solve the adjoint equation for the FEM part:

$$\frac{\partial \mathbf{R}_{\text{FEM}}}{\partial \mathbf{w}_{\text{FEM}}}^T \mathbf{\Psi}_{\text{FEM}} = \frac{\partial f}{\partial \mathbf{w}_{\text{FEM}}}^T,\tag{14}$$

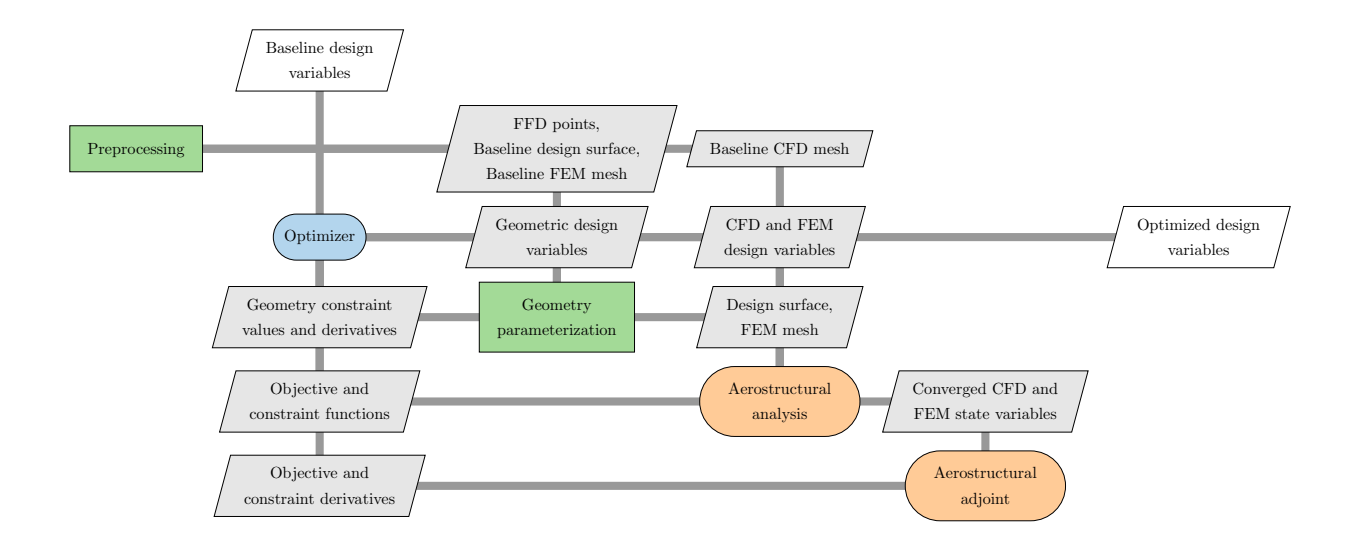


Fig. 2 Schematic of aerostructural optimization using OpenMDAO/MPhys [20]. Here we use the XDSM representation. The diagonal blocks are the components, and the off-diagonal blocks are data transfers. The aerostructural analysis component is detailed in Fig. 1, and the aerostructural coupled adjoint is elaborated on in Sec. II.E.

The matrix-vector product for the off-diagonal components is computed by using a matrix-free manner through automatic differentiation.

Traditionally, the above aerostructural coupling is implemented in a solver-specific manner and is hard to extend. By leveraging the flexibility of OpenMDAO and MPhys, the aerostructural is implemented in a modular manner. In MPhys, we need to implement the methods to compute the output based on the input for the components shown in Fig. 1, as well as the product of the state Jacobian matrix with a given vector. OpenMADO will then use the MAUD algorithm [37] to unify the adjoint total derivative computation. The CFD and FEM coupled adjoint is solved using the linear block Gauss–Seidel solver with Aitken relaxation in OpenMDAO.

#### F. Aerostructural Optimization Framework

Figure 2 shows the schematic of the aerostructural optimization framework under the OpenMDAO/MPhys [20] framework. In the "Preprocessing" step, we generate the "CFD mesh" and "FEM mesh" for the "Baseline design surface" geometry. We also generate the free-form deformation (FFD) control points for geometry parameterization. Then, the "Optimizer" (SNOPT [38]) will pass the initial "Geometric design variables" (FFD points displacement) to the "Geometry parameterization" module pyGeo. pyGeo [39] is an open-source FFD tool to parameterize the design surface geometry. pyGeo can embed a set of point clouds into the prescribed FFD box and then deform the point cloud by moving the FFD coordinates. pyGeo works for structured and unstructured meshes. The FFD box generated in the preprocessing step will fully contain the CFD design surface and surface mesh. Next, the "Updated design surface" is passed to the "Aerostructural analysis" component. The aerostructural analysis component will then solve the flow and send the "Converged state variables" to the "Aerostructural adjoint" component. It also computes the aerostructural "Objective and constraint functions" (e.g., power, thrust, von Mises stress). Finally, the "Aerostructural adjoint" computes the total derivatives of the objective and constraint functions and passes them back to the "Optimizer". The "Optimizer" will use the function values and derivatives to update the design variables for the next optimization iteration. The above process will repeat until the optimization converges.

# III. Results and Discussion

In this section, we show the aerostructural optimization results. We consider three different configurations with various combinations of design variables, including the propeller twist, shape, chord, span, and rotation speed.

#### A. Aerostructural analysis and optimization configurations

Figure 3 shows the CFD and FEM meshes for the propeller blade. A summary of the propeller geometry, materials, and working conditions is shown in Table 1. We use Pointwise to generate an unstructured mesh with about 1,190,000 cells with an average  $y^+ \approx 0.7$ . For structural consideration, we mesh both the propeller blade and the spinner. In addition, we add a rounded fillet at the root of the blade to avoid stress concentration. The propeller has two blades; however, we simulate only one with periodic boundary faces. For structural simulations, we generate an unstructured triangulated mesh with about 493,000 cells using ICEM CFD. We use the CTETRA linear solid element type. We plan to 3D print the designs for experimental validation. So we use the VeroWhite as the blade material, and its properties are density 1170 kg/m³, elastic modulus 2500 MPa, Poisson's ratio 0.3, and yield stress 70 MPa. We impose zero displacement and rotation conditions on the inner and periodic faces of the spinner.

The simulation domain is a half-cylinder (Fig. 3). At the inlet, outlet, and outer patches, we impose the total pressure and total temperature boundary conditions. The propeller is rotating at 5000 RPM. The propeller has a radius of 0.15 m, and the tip speed is 78.5 m/s. The Reynolds number, which is based on the chord and blade rotation speed at 75% span, is 1.8×10<sup>5</sup>. As mentioned above, we use OpenFOAM's rhoSimpleFoam solver with the MRF approach to simulate the steady-state turbulent flow with rotation. The turbulence model is Spalart–Allmaras. We select all mesh cells in the simulation domain as the rotating zone.

Table 3 shows the aerostructural optimization problem formulation. We use the propeller shaft power coefficient as the objective function, which is defined as:

$$C_P = \frac{P}{\rho n^3 D^5} \tag{15}$$

where P is the shaft power.  $\rho$  is the far field reference density, n is the rotation speed in revolution per second, and D is the blade outer diameter. We set two body-fitted FFD boxes for the propeller blade and spinner, as shown in Fig. 3. Only the blue FFD points for the blade are allowed to move during the optimization. To avoid poor mesh quality at the blade root, we fix the first to third layers of the blue FFD points in the spanwise direction. In other words, only the fourth and higher blue FFD points (a total of six FFD spanwise sections) can move during the optimization. The design variables include the blade's sectional shape, twist, chord, span, and rotation speed. To study the impacts of selecting various combinations of design variables on the optimization results, we consider three optimization configurations, as shown in Table 2. Here we gradually add more design variables and compare the optimization results among these configurations. The most complicated case (Configuration 3) has up to 86 design variables.

To ensure a feasible propeller design, we impose both physical and geometrical constraints. We require the thrust coefficient to remain constant during the optimization. The definition of thrust coefficient is:

$$C_T = \frac{T}{\rho n^2 D^4} \tag{16}$$

where *T* is the thrust. We also impose blade thickness constraints to prevent the blade thickness from being too thin. To this end, we enforce the thickness at 200 blade locations to be within 0.8 to 3 of its baseline thickness. To ensure good mesh quality during the optimization, we impose two mesh quality constraints for the volume mesh deformation. The maximal non-orthogonality and skewness are constrained to be less than 80° and 4, respectively. The mesh quality values are computed using OpenFOAM's built-in checkMesh utility and DAFoam has a flexible interface to compute the constraints' derivatives with respect to the design variables through automatic differentiation. Moreover, we impose a spanwise curvature constraint to prevent a wavy shape in the spanwise, similar to what we used in the previous wing aerodynamic optimization study [10]. The spanwise curvature of the blade is constrained to no more than 1.5 times the baseline curvature. We impose a mass constraint such that the optimized blade is no more than 10% heavier than the baseline design. Moreover, we require the maximal von Mises stress in the blade to be less than 50% of the yield stress. The maximal stress is approximated by aggregating the stress constraint value using the Kreisselmeier–Steinhauser (KS) function. In total, we have 217 constraints. All three optimization configurations use the same constraints.

Figure 4 shows the blade pressure contours for the baseline design. We observe a high-pressure difference region near the tip, which suggests that the loading at the tip is higher than at the root. This is expected because of the higher rotation speed at the tip. Figure 5 compares undeformed and structurally deformed blade geometry for the baseline design. As expected, the propeller blade bends against the flow direction under the aerodynamic load. The deformation in the flow (x) direction is about 7% of the blade tip radius. This justifies the need to consider aerostructural coupling in propeller design optimization. Our optimization framework will consider the aerodynamic performance of the structurally deformed blade instead of assuming the blade will remain rigid under the aerodynamic load. In the following, we will analyze the optimization results for the above three configurations.

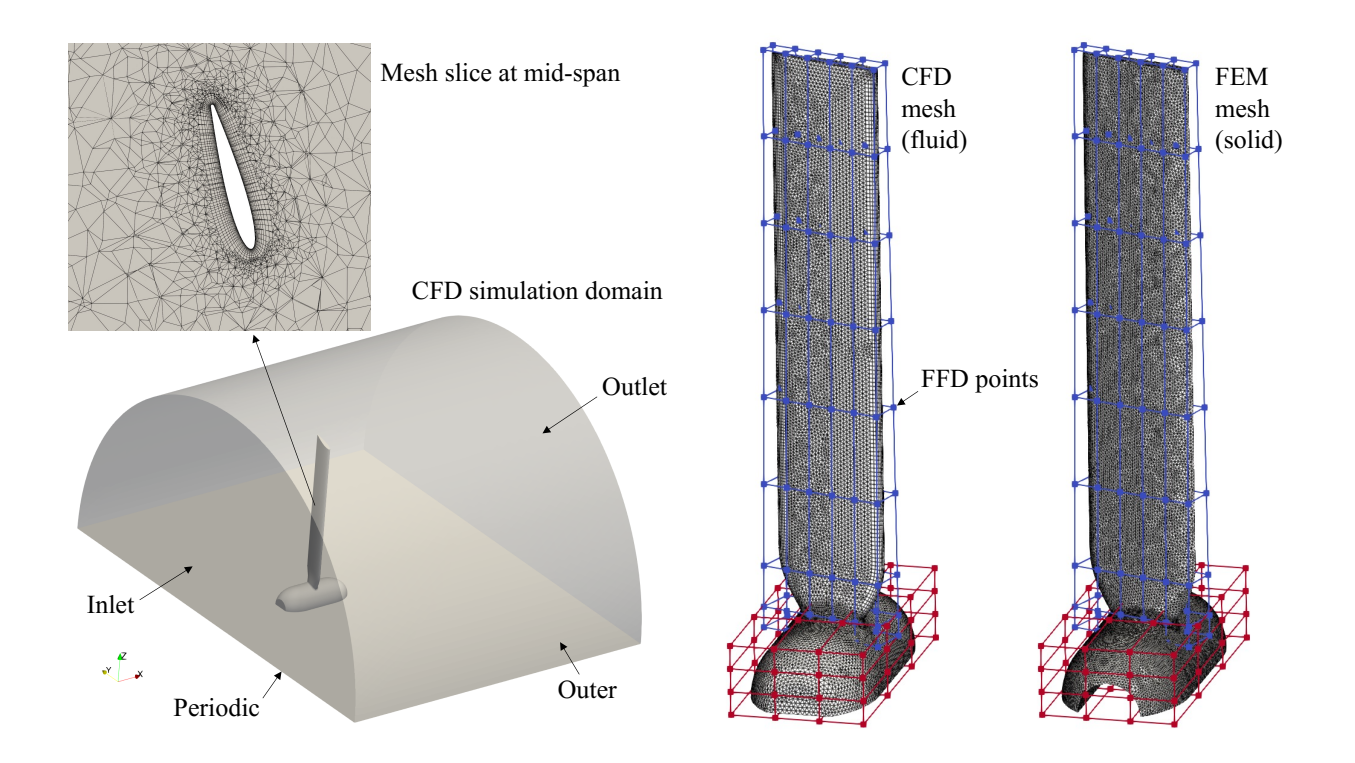


Fig. 3 Simulation domain, propeller meshes, and FFD points. The CFD and FEM meshes are generated using Pointwise and ICEM-CFD, respectively. The blue and red squares are the FFD points. Only the blue FFD points move during the optimization.

Table 1 Summary of the propeller geometry, materials, and working conditions.

Parameters	Value
rarameters	value
Blade profile	NACA0012
Planform	Untwisted & untapered
Number of blades	2
Tip radius $(R)$	0.15 m
Tip/root ratio $(r/R)$	0.1
Chord/tip ratio $(c/R)$	0.3
Pitch angle	15°
Working condition	Hover
Rotation speed	5000 RPM
Blade material	VeroWhite
Density	$1170 \text{ kg/m}^3$
Elastic modulus	2500 MPa
Poisson ratio	0.33
Yield stress	70 MPa

### **B.** Configuration 1: Twist-only

The first optimization configuration uses only the 6 spanwise twists as the design variables. The optimization runs for 18 iterations, and the optimization two orders of magnitude. Table 4 summarizes the optimization results for this configuration. We obtain 10.2% power reduction, and the thrust, mass, and stress constraints are satisfied. Because we run the optimization at a fixed thrust level ( $C_T \approx 0.094$ ), it is unclear whether the optimized propeller outperforms the

Table 2 Summary of the three optimization configurations. All configurations use the same constraints.

Config.	Design variables
1	Twist
2	Twist, shape, and chord
3	Twist, shape, chord, span, and rotation speed

Table 3 Aerostructural optimization problem formulation. The superscript bl denotes the baseline design. We use up to 86 design variables and 217 constraints.

	Function/Variable	Description	Quantity
Minimize	$C_P$	Propeller shaft power coefficient	
with respect to	$-50^{\circ} \le \gamma \le 50^{\circ}$	Propeller sectional twists	6
	$-0.05 \text{ m} \le \Delta x \le 0.05 \text{ m}$	Propeller sectional shape	72
	$0.5 \le c/c^{\rm bl} \le 2.0$	Propeller sectional chord	6
	$-0.1 \text{ m} \le \Delta s \le 0.1 \text{ m}$	Propeller span	1
	$0.8 \le \omega/\omega^{\rm bl} \le 1.2$	Propeller rotation speed	1
		<b>Total Design Variables</b>	86
subject to	$C_T = C_T^{\text{bl}}$	Thrust constraint	1
	$0.8t^{\rm bl} \le t \le 3t^{\rm bl}$	Propeller thickness constraint	200
	$C \le 1.5C^{\mathrm{bl}}$	Propeller spanwise curvature constraint	2
	$R_{\rm LE} \geq 0.8 R_{\rm LF}^{\rm bl}$	Propeller leading edge radius	10
	$\theta \le 80^{\circ}$	Max mesh non-orthogonality	1
	$\mu \leq 4$	Max mesh skewness	1
	$m \leq 1.1 m^{\rm bl}$	Propeller mass constraint	1
	$\sigma/\sigma_{\rm yield} \le 0.5$	Max von Mises stress constraint	1
	-	<b>Total Constraint Functions</b>	217

Sunction side Pressure side

Cp
-2.0 -1.5 -1.0 -0.5 0.0 0.5 1.0 1.5

Fig. 4 Pressure contours for the baseline design.

baseline design at other thrust levels. To verify the above point, we extract the baseline and optimized blade geometries and then run aerostructural analysis at various thrust levels, ranging from  $C_T = 0.083$  to 0.098, as shown in Fig. 6. The optimized design outperforms the baseline one at all thrust levels. We also observe that the power reduction at high-thrust conditions is higher than that for low-thrust conditions.

To further analyze the optimization result, we plot the pressure contour for the optimized design in Fig. 7. Compared with the baseline design (Fig. 4), the low-pressure region is smaller near the tip for the optimized design. This indicates that the pressure load is lower in the optimized design than in the baseline design at the tip. To better illustrate this, we

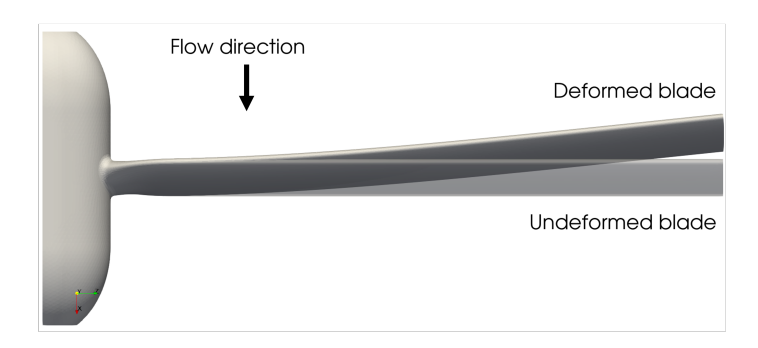


Fig. 5 Comparison of the undeformed and structurally deformed blade geometries for the baseline design. Due to the pressure load, the propeller blade bends against the flow direction.

Table 4 Summary of aerostructural optimization for Twist-only case (configuration 1). We obtain 10.2% power reduction, and the thrust, mass, and stress constraints are satisfied.

	Baseline Design	Optimized Design
$C_P$	0.0481	0.0432 (\ 10.2%)
$C_T$	0.0943	0.0948
m, kg	0.0564	0.0562
$\sigma/\sigma^{ m yield}$	0.0424	0.0369

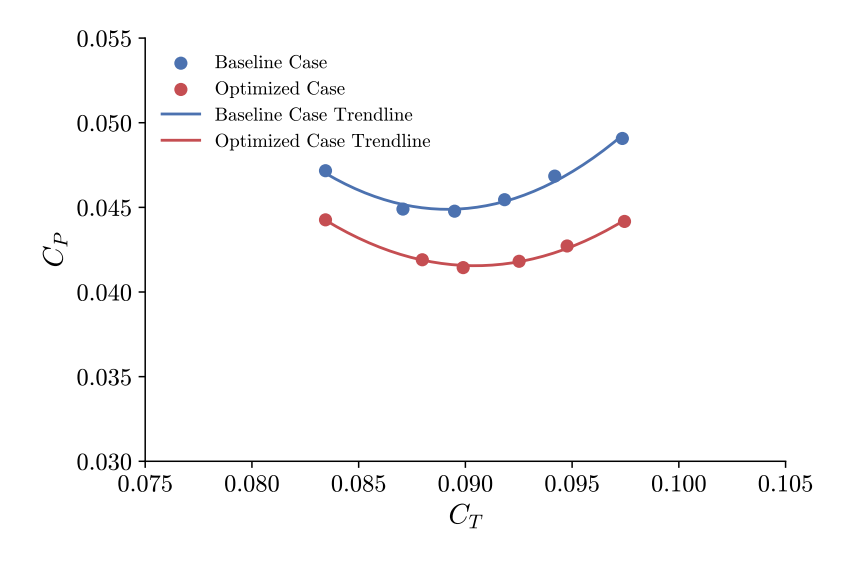


Fig. 6 Thrust vs power for the baseline and optimized designs (Twist-only; optimization configuration 1).

plot the pressure distributions at the tip and mid-span for the baseline and optimized designs in Fig. 8 right. It is evident that the pressure load decreases at the tip but increases at the mid-span in the optimized design. Figure 8 left shows the comparison of 3D blade geometries for the baseline and optimized designs. We observe a large twist near the root in the optimized design, which contributes to the increasing pressure load in the mid-span (Fig. 8 right).

To better illustrate the spanwise distribution of aerodynamic and geometry variables for the blade, we plot the spanwise thrust and twist profiles in Fig. 9. Consistent with the previous observations, the baseline design has a relatively higher thrust (blade loading) near the tip. For the optimized design, the thrust at the tip is lower but distributes more evenly along the span. The max thrust is located at 90% and 80% span for the baseline and optimized designs,

Sunction side Pressure side

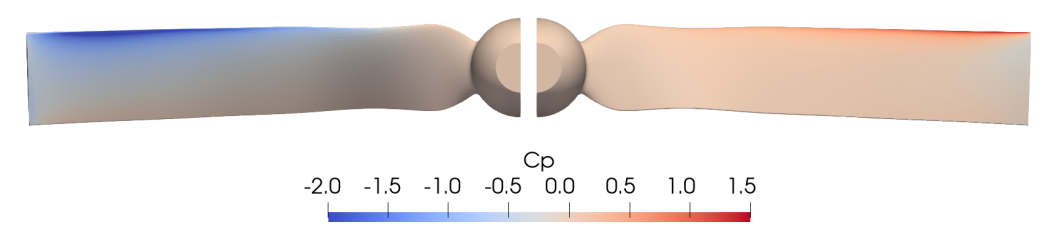


Fig. 7 Pressure contour for the optimized design (Twist-only; Configuration 1).

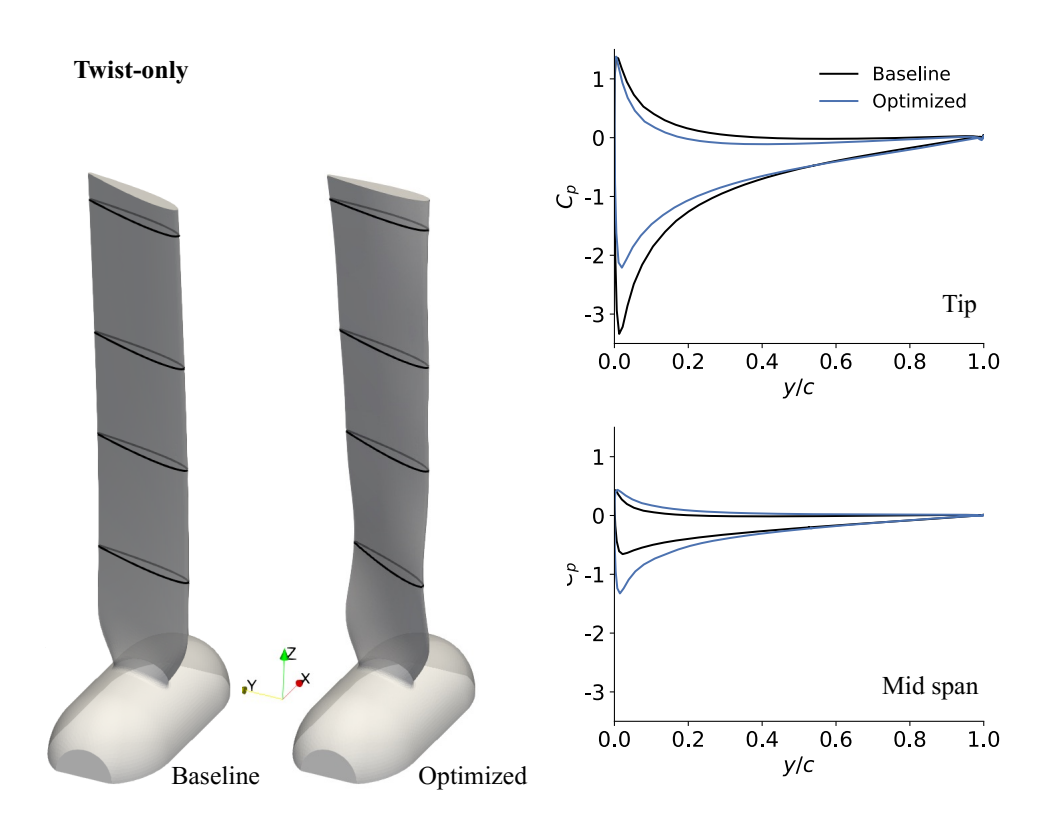


Fig. 8 Left: geometries of the baseline and optimized blades (Twist-only; configuration 1). Right: Pressure distributions at the tip and mid-span for the baseline and optimized designs.

respectively. This re-distribution of spanwise thrust is mainly achieved by twisting the blade, as shown in Fig. 9 right. The twist decreases from 27 degrees at the 20% span to 5 degrees at the tip. Unlike wing aerodynamic optimization, where the incoming flow is in a constant direction, the incoming velocity direction for propellers varies along the span. The blade twist distribution is a critical design variable that optimizes the angle of attack of each airfoil section along the span and minimizes the blade profile loss. The trend of the optimized spanwise twist is consistent with human intuition-based designs such as [40, 41].

## C. Configuration 2: Twist+Shape+Chord

The second optimization configuration uses two more design variables (shape and chord) than the first configuration. All other optimization settings (e.g., objective function and constraints) are the same. The optimization runs for 42 iterations, and the optimization one order of magnitude. Table 5 summarizes the optimization results for this configuration. We obtain 18.3% power reduction, and the thrust, mass, and stress constraints are satisfied. Compared

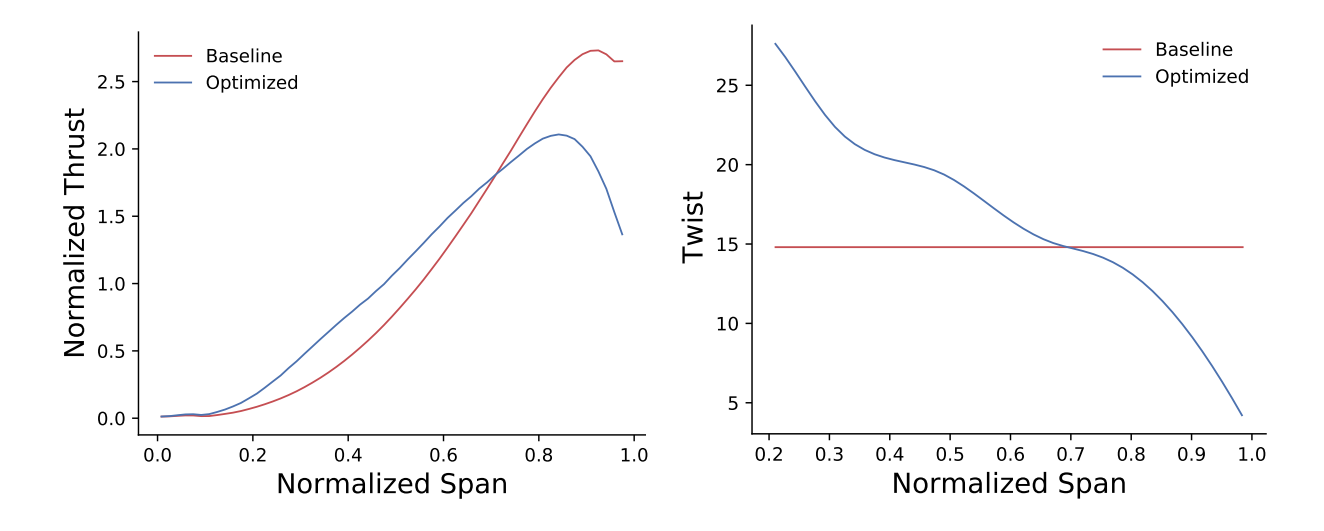


Fig. 9 Spanwise distributions of thrust (left) and twist (right) for the baseline and optimized designs (Twist-only; Configuration 1).

Table 5 Summary of aerostructural optimization for Twist+Shape+Chord case (configuration 2). We obtain 18.3% power reduction, and the thrust, mass, and stress constraints are satisfied.

	Baseline Design	Optimized Design
$C_P$	0.0481	0.0393 (\ 18.3%)
$C_T$	0.0943	0.0956
m, kg	0.0564	0.0532
$\sigma/\sigma^{ m yield}$	0.0424	0.0317

with configuration 1 (twist-only), we get 8.1% more power reduction, which is expected because we have more design freedom in configuration 2. Figure 10 shows the variation of power coefficient with respect to the thrust coefficient for the baseline and optimized designs. Similar to what we observed for the twist-only case, the optimized design outperforms the baseline design at all thrust levels, which confirms the success of the optimization. However, the amount of power reduction in the optimized designs increases at the lower thrust level, i.e.,  $C_T < 0.085$ . This trend is different from what we observed in the twist-only case (Fig. 6).

To further analyze the optimization results, we plot the pressure contours on the pressure and suction sides for the optimized blade in Fig. 11. The optimized design decreases the chord at the tip and increases the chord at 30% span, a chord distribution similar to many existing human intuition-based designs, e.g., [25, 40]. Moreover, we find that the optimized design's pressure difference at the tip is much lower than the baseline design and twist-only optimized design's pressure difference, indicating that the aerodynamic load is further decreased at the tip for the Twist-Shape-Chord configuration. To further confirm this trend, we plot the pressure profiles at the tip and mid-span in Fig. 12. Overall, the optimized design's pressure load is much lower than the baseline design's at the tip. As shown in Fig. 12 right, the pressure load at the tip is reduced at the leading edge and distributes more smoothly along the chord. This is achieved by twisting the blade at the tip and using cambered sectional airfoil profiles in the Twist-Shape-Chord case. However, at the mid-span, the optimized design's pressure load is higher than the baseline design's. Similar to the Twist-only case, we observe a high twist at about 30% span location in the optimized design, which further contributes to the increased pressure load. This overall trend of load redistribution is more clearly seen in Fig. 13, where the spanwise distributions of thrust and twist are plotted. Compared with the twist-only case, the peak thrust is further reduced in the Twist-Shape-Chord optimized design. Figure 13 right shows the spanwise twist distribution. Similar to the twist-only case, the optimized twist in configuration 2 decreases along the span.

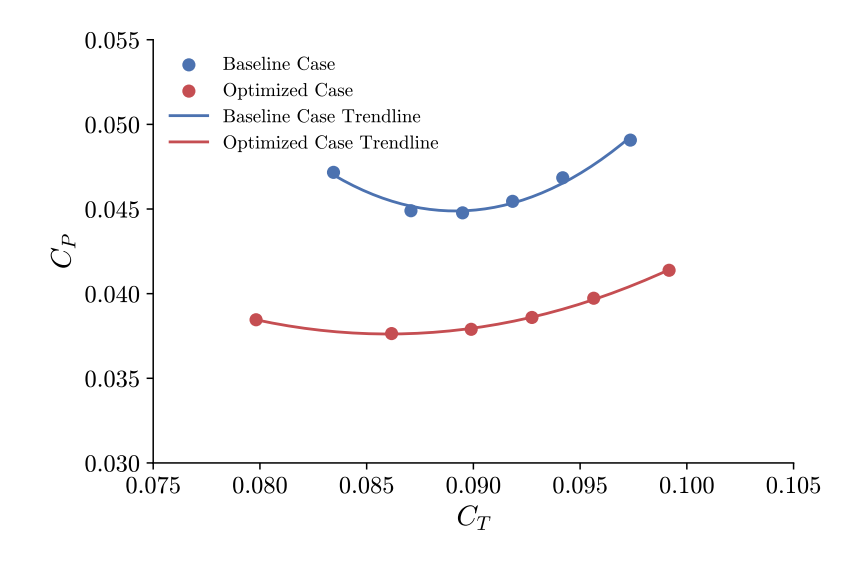


Fig. 10 Thrust vs power for the baseline and optimized designs (Twist-Shape-Chord; optimization configuration 2).

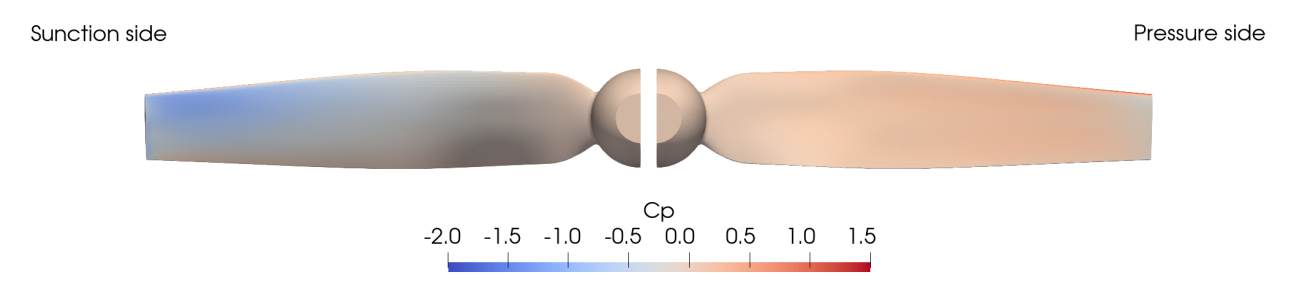


Fig. 11 Pressure contour for the optimized design (Twist-Shape-Cord; Configuration 2).

## D. Configuration 3: Twist+Shape+Chord+Span+Rotation

In the final optimization, we allow two more design variables to change, i.e., the blade span and rotation speed. The configuration is slightly different from others because the variables that normalize the objective and constraint functions, i.e.,  $C_T$  and  $C_P$ , are changing during the optimization. To enable this, we create an OpenMDAO component that receives the power, thrust, rotation speed, and blade outer radius as the inputs and output  $C_T$  and  $C_P$ . The power and thrust are obtained from the CFD solver, the rotation speed is an independent design variable, and the outer radius is computed using a sample point from the CFD mesh at the blade tip. All the inputs from the above components can change during the optimization, and the optimizer dynamically adjusts their values to maintain a constant  $C_T$  while minimizing  $C_P$ . The optimization runs for 38 iterations, and the optimality drops half an order of magnitude.

This configuration has the highest design freedom and is expected to have the largest power reduction, which can be confirmed in Table. 6. The power coefficient is reduced by 21.4% in the optimized design, which is 3.1% more than the Twist-Shape-Chord configuration. By comparing the results in configurations 1 to 3, we conclude that the twist is the most important design variable for power reduction. Moreover, both the blade rotation speed and span increase during the optimization, which indicates that the thrust (T) in the optimized design is much higher than the baseline design. Note that the blade mass increases in the optimized design, but it is still within the constraint bound (i.e.,  $m \le 1.1 m^{\rm bl}$ ; Table 3); all constraints are satisfied.

Figure 14 shows the variation of power coefficient with respect to the thrust coefficient for the baseline and optimized designs. Similar to what we observed in the previous cases, the optimized design outperforms the baseline design at all thrust levels, which confirms the success of the optimization. However, we observe that the optimized design's power reduction is much higher in the low-thrust region than in the high-thrust one. This trend is different from what we

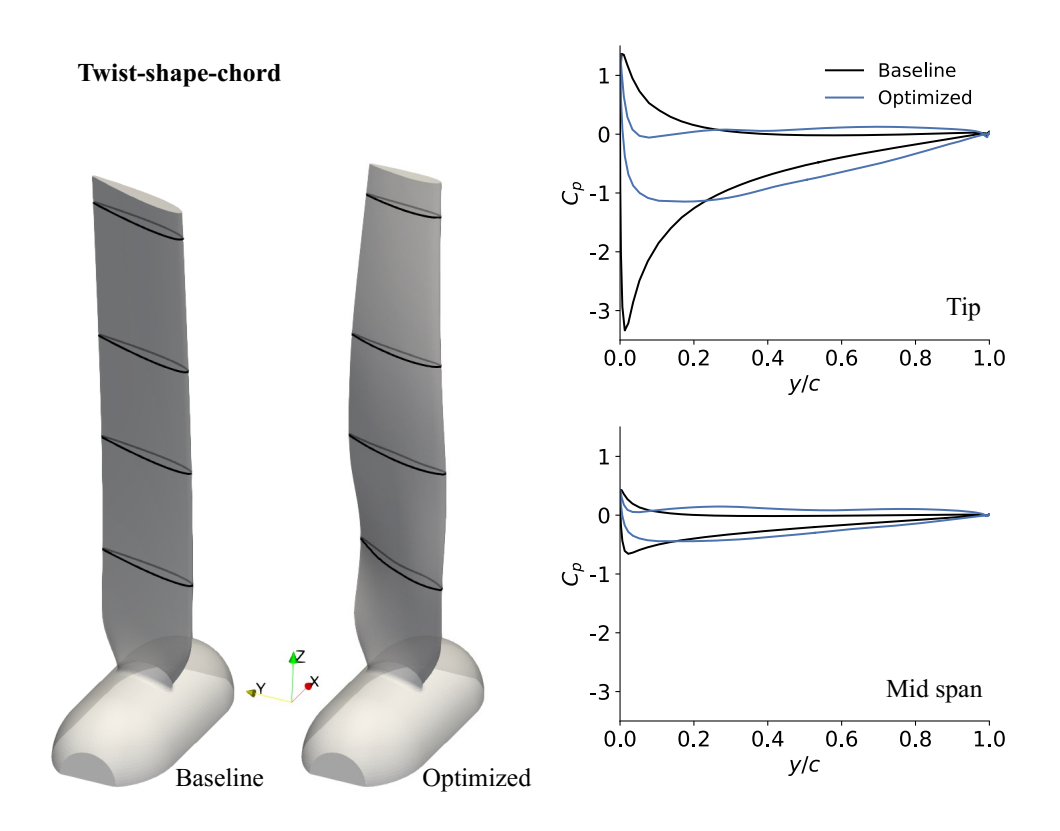


Fig. 12 Left: geometries of the baseline and optimized blades (Twist-Shape-Chord; configuration 2). Right: Pressure distributions at the tip and mid-span for the baseline and optimized designs.

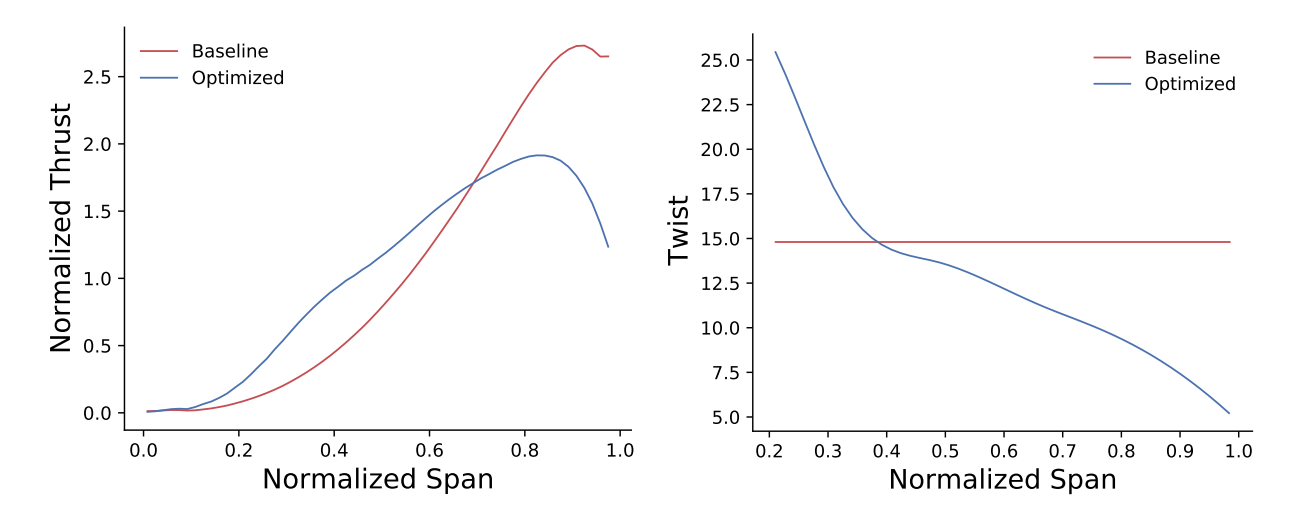


Fig. 13 Spanwise distributions of thrust (left) and twist (right) for the baseline and optimized designs (Twist-Shape-Chord; Configuration 2).

observed in the twist-only case (Fig. 6) and twist-shape-chord case (Fig. 10). We speculate this is due to the increased blade span during the optimization.

To further analyze the results, we plot the pressure contours on the pressure and suction sides for the Twist-Shape-Cord-Span-Rotation optimized design in Fig. 15. A high-pressure difference (blade loading) region is near the blade tip.

Table 6 Summary of aerostructural optimization for Twist+Shape+Chord+Span case (configuration 3). We obtain 21.4% power reduction, and the thrust, mass, and stress constraints are satisfied.

	Baseline Design	Optimized Design
$C_P$	0.0481	0.0378 (\ 21.4%)
$C_T$	0.0943	0.0934
m, kg	0.0564	0.0621
$\sigma/\sigma^{ m yield}$	0.0424	0.0317
s, m	0.150	0.186
$\omega$ , rad/s	523.6	530.7
<i>T</i> , N	6.50	15.62

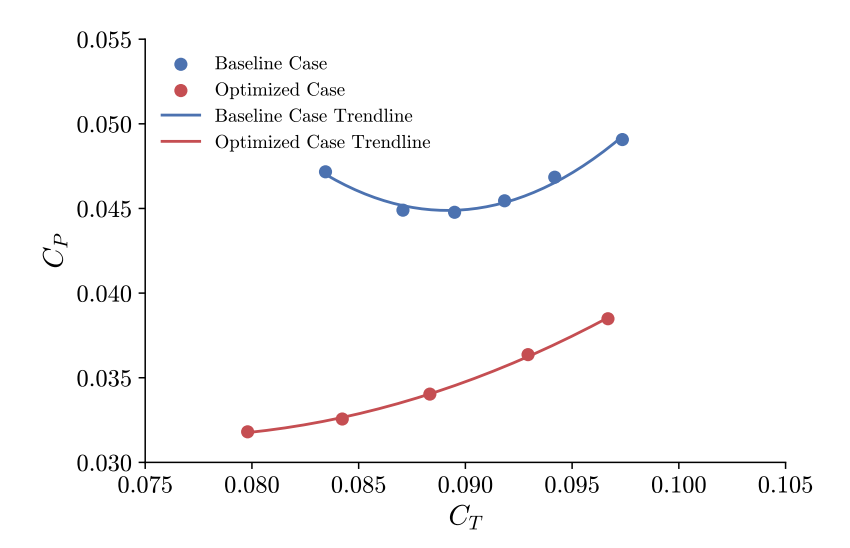


Fig. 14 Thrust vs power for the baseline and optimized designs (Twist-Shape-Chord-Span-Rotation; optimization configuration 3).

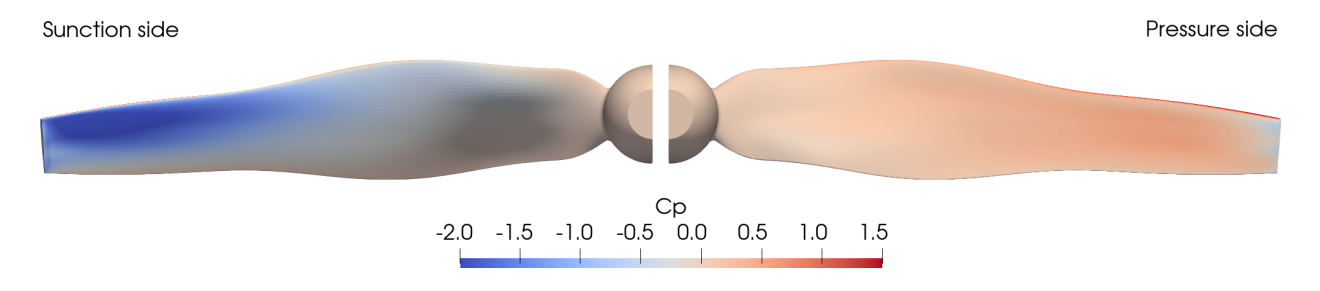


Fig. 15 Pressure contour for the optimized design (Twist-Shape-Cord-Span-Rotation; Configuration 3).

The blade loading and the integral thrust are much higher than the previous two configurations. This is consistent with what we observe in Table 6. We also notice that the optimizer decreases the chord at the tip and increases it near the 30% span. Figure 16 shows the geometries of the baseline and optimized blades and the pressure distributions at the tip and midspans. The left sub-figures further confirm that the pressure difference significantly increases at the tip. Moreover, we also observe a large twist at 20%, which contributes to the increased pressure difference near the midspan. Finally, we plot the spanwise distributions of thrust (left) and twist (right) for the baseline and optimized designs for this

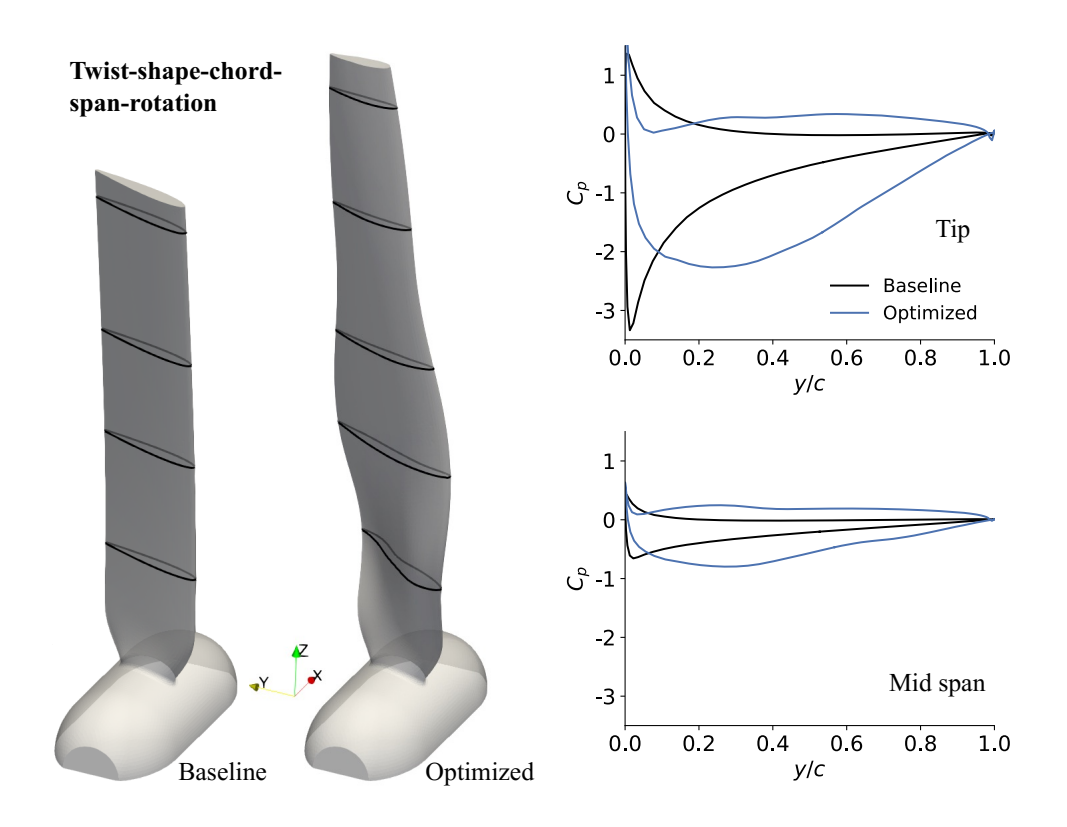


Fig. 16 Left: geometries of the baseline and optimized blades (Twist-Shape-Chord-Span-Rotation; configuration 3). Right: Pressure distributions at the tip and mid-span for the baseline and optimized designs.

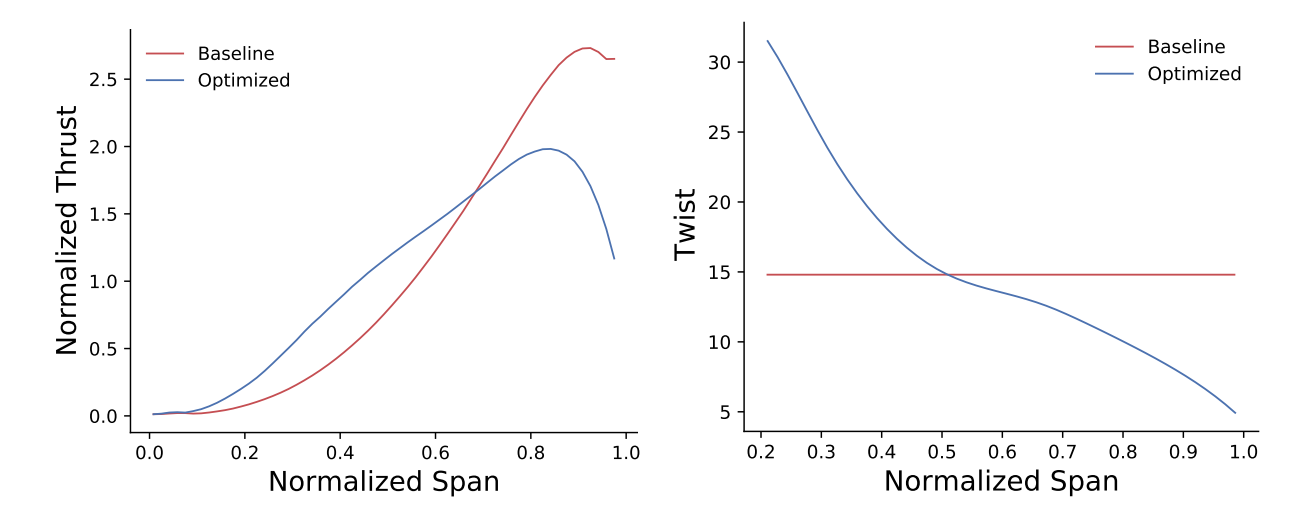


Fig. 17 Spanwise distributions of thrust (left) and twist (right) for the baseline and optimized designs (Twist-Shape-Chord-Span-Rotation; Configuration 3).

configuration. The optimized design redistributes the thrust profile, making the thrust distribute more smoothly along the span. Note that we normalize the thrust in this plot, so the actual thrust (N) in the optimized design is much higher than the baseline design. The optimized twist decreases along the span, as shown in Figure 17 right.

## **IV. Conclusion**

In this paper, we propose an aerostructural optimization benchmark for aircraft propellers. We use a high-fidelity CFD solver (OpenFOAM) to simulate the flow and a FEM solver (TACS) to simulate the structure. We then use the discrete adjoint approach to compute the derivatives of objective and constraint functions with respect to a large number of design variables and constraints using DAFoam (fluid) and TACS (structure). The adjoint method allows us to have large design freedom for performance improvement. The fluid-structure interaction and its derivative computation are conducted based on NASA's OpenMDAO/MPhys framework.

We use an untwisted and untapered blade with the NACA0012 airfoil profile as the baseline. The blade is working in a hover condition. The objective function is the propeller shaft power coefficient. The design variables include the propeller twist, shape, chord, span, and rotation speed. The constraints include the propeller thrust coefficient, mass, von Mises stress, and geometry (e.g., thickness and curvature). We propose three different optimization configurations with various combinations of design variables. Configuration 1: Twist-only, configuration 2: twist-shape-chord, and configuration 3: twist-chord-span-rotation. The optimization shows that the blade deforms under the pressure load and it is important to consider the structural deformation during the optimization. The twist is the most important design variable and optimizing it alone achieves a 10.2% power reduction. Adding blade sectional shape and chord as design variables gives us 8.1% more power reduction. Finally, allowing the span and blade rotation speed to change provides 3.1% more power reduction. Overall, all optimized designs outperform the baseline design at all thrust levels. However, we observe that configuration 3 exhibits better performance at low thrust levels.

# Acknowledgments

This material is based upon work supported by the National Science Foundation under Grant Number 2223676.

#### References

- [1] Martins, J. R. R. A., and Lambe, A. B., "Multidisciplinary design optimization: A survey of architectures," *AIAA Journal*, Vol. 51, No. 9, 2013, pp. 2049–2075. https://doi.org/10.2514/1.J051895, iSBN: 10.2514/1.J051895.
- [2] Martins, J. R. R. A., and Ning, A., Engineering design optimization, Cambridge University Press, 2021.
- [3] Jameson, A., Martinelli, L., and Pierce, N. A., "Optimum aerodynamic design using the Navier–Stokes equations," *Theoretical and Computational Fluid Dynamics*, Vol. 10, No. 1–4, 1998, pp. 213–237. https://doi.org/10.1007/s001620050060.
- [4] Giles, M. B., Duta, M. C., M-uacute, J.-D., Ller, and Pierce, N. A., "Algorithm developments for discrete adjoint methods," *AIAA Journal*, Vol. 41, No. 2, 2003, pp. 198–205. https://doi.org/10.2514/2.1961, iSBN: 0001-1452.
- [5] Peter, J. E. V., and Dwight, R. P., "Numerical sensitivity analysis for aerodynamic optimization: A survey of approaches," *Computers and Fluids*, Vol. 39, No. 3, 2010, pp. 373–391. https://doi.org/10.1016/j.compfluid.2009.09.013.
- [6] Kenway, G. K., Mader, C. A., He, P., and Martins, J. R., "Effective adjoint approaches for computational fluid dynamics," Progress in Aerospace Sciences, Vol. 110, 2019, p. 100542. https://doi.org/10.1016/j.paerosci.2019.05.002, publisher: Pergamon.
- [7] Reuther, J., Jameson, A., Farmer, J., Martinelli, L., and Saunders, D., "Aerodynamic shape optimization of complex aircraft configurations via an adjoint formulation," *Proceedings of the 34th AIAA aerospace sciences meeting and exhibit*, Reno, Nevada, 1996.
- [8] Kenway, G. K. W., and Martins, J. R. R. A., "Multipoint high-fidelity aerostructural optimization of a transport aircraft configuration," *Journal of Aircraft*, Vol. 51, No. 1, 2014, pp. 144–160. https://doi.org/10.2514/1.C032150.
- [9] Lyu, Z., Kenway, G. K. W., and Martins, J. R. R. A., "Aerodynamic shape optimization investigations of the Common Research Model wing benchmark," *AIAA Journal*, Vol. 53, No. 4, 2015, pp. 968–985. https://doi.org/10.2514/1.J053318.
- [10] Koyuncuoglu, H. U., and He, P., "Simultaneous wing shape and actuator parameter optimization using the adjoint method," *Aerospace Science and Technology*, Vol. 130, 2022, p. 107876. Publisher: Elsevier.
- [11] Dhert, T., Ashuri, T., and Martins, J. R. R. A., "Aerodynamic shape optimization of WIND TURBINE blades using a Reynolds-averaged Navier–Stokes model and an adjoint method," *Wind Energy*, Vol. 20, No. 5, 2017, pp. 909–926. Publisher: Wiley Online Library.

- [12] Madsen, M. H. A., Zahle, F., Sørensen, N. N., and Martins, J. R. R. A., "Multipoint high-fidelity CFD-based aerodynamic shape optimization of a 10 MW wind turbine," Wind Energy Science, Vol. 4, 2019, pp. 163–192. https://doi.org/10.5194/wes-4-163-2019.
- [13] Wang, D. X., and He, L., "Adjoint aerodynamic design optimization for blades in multistage turbomachines—Part I: Methodology and verification," *Journal of Turbomachinery*, Vol. 132, No. 2, 2010, p. 21011. Publisher: American Society of Mechanical Engineers.
- [14] Ma, C., Su, X., and Yuan, X., "An efficient unsteady adjoint optimization system for multistage turbomachinery," *Journal of Turbomachinery*, Vol. 139, No. 1, 2017, p. 11003. Publisher: American Society of Mechanical Engineers.
- [15] He, P., Martins, J. R. R. A., Mader, C. A., and Maki, K., "Aerothermal optimization of a ribbed U-Bend cooling channel using the adjoint method," *International Journal of Heat and Mass Transfer*, Vol. 140, 2019, pp. 152–172. https://doi.org/10.1016/j. ijheatmasstransfer.2019.05.075.
- [16] He, P., Mader, C. A., Martins, J. R. R. A., and Maki, K. J., "Aerothermal optimization of internal cooling passages using a discrete adjoint method," *AIAA/ASME joint thermophysics and heat transfer conference*, Atlanta, GA, 2018. https://doi.org/10.2514/6.2018-4080.
- [17] Hwang, J. T., and Ning, A., "Large-scale multidisciplinary optimization of an electric aircraft for on-demand mobility," 2018 AIAA/ASCE/AHS/ASC Structures, Structural Dynamics, and Materials Conference, No. January, 2018, pp. 1–18. https://doi.org/10.2514/6.2018-1384, iSBN: 978-1-62410-532-6.
- [18] Moore, K. R., and Ning, A., "Takeoff and performance trade-offs of retrofit distributed electric propulsion for urban transport," *Journal of Aircraft*, Vol. 56, No. 5, 2019, pp. 1880–1892. https://doi.org/10.2514/1.c035321, publisher: American Institute of Aeronautics and Astronautics.
- [19] Gray, J. S., Hwang, J. T., Martins, J. R. R. A., Moore, K. T., and Naylor, B. A., "OpenMDAO: An open-source framework for multidisciplinary design, analysis, and optimization," *Structural and Multidisciplinary Optimization*, 2019.
- [20] "Mphys code,", 2022. URL https://github.com/OpenMDAO/mphys.
- [21] He, P., Mader, C. A., Martins, J. R. R. A., and Maki, K. J., "An aerodynamic design optimization framework using a discrete adjoint approach with OpenFOAM," *Computers & Fluids*, Vol. 168, 2018, pp. 285–303. https://doi.org/10.1016/j.compfluid. 2018.04.012.
- [22] He, P., Mader, C. A., Martins, J. R. R. A., and Maki, K. J., "DAFoam: An open-source adjoint framework for multidisciplinary design optimization with OpenFOAM," *AIAA Journal*, Vol. 58, No. 3, 2020, pp. 1304–1319. https://doi.org/10.2514/1.J058853.
- [23] He, P., Mader, C. A., Martins, J. R. R. A., and Maki, K., "An object-oriented framework for rapid discrete adjoint development using OpenFOAM," *AIAA scitech 2019 forum*, American Institute of Aeronautics and Astronautics, Reston, Virginia, 2019. https://doi.org/10.2514/6.2019-1210.
- [24] Pacini, B., Prajapati, M., Duraisamy, K., Martins, J. R., and He, P., "Towards mixed-fidelity aero-structural-acoustic optimization for urban air mobility vehicle design," AIAA AVIATION 2023 forum, American Institute of Aeronautics and Astronautics, Reston, Virginia, 2023. https://doi.org/10.2514/6.2023-3905.
- [25] He, P., Koyuncuoglu, H., Hu, H., Dhulipalla, A., Hu, H., and Hu, H., "High-fidelity aerodynamic and aerostructural optimization of UAV propellers using the adjoint method," *AIAA SCITECH 2023 forum*, American Institute of Aeronautics and Astronautics, Reston, Virginia, 2023. https://doi.org/10.2514/6.2023-0531.
- [26] Weller, H. G., Tabor, G., Jasak, H., and Fureby, C., "A tensorial approach to computational continuum mechanics using object-oriented techniques," *Computers in Physics*, Vol. 12, No. 6, 1998, pp. 620–631. Publisher: AIP Publishing.
- [27] Spalart, P., and Allmaras, S., "A one-equation turbulence model for aerodynamic flows," *30th aerospace sciences meeting and exhibit*, 1992. https://doi.org/10.2514/6.1992-439.
- [28] Kennedy, G. J., and Martins, J. R., "A parallel finite-element framework for large-scale gradient-based design optimization of high-performance structures," *Finite Elements in Analysis and Design*, Vol. 87, 2014, pp. 56–73. https://doi.org/10.1016/j.finel. 2014.04.011, publisher: Elsevier.
- [29] Mader, C. A., Kenway, G. K. W., Yildirim, A., and Martins, J. R. R. A., "ADflow—An open-source computational fluid dynamics solver for aerodynamic and multidisciplinary optimization," *Journal of Aerospace Information Systems*, 2020. https://doi.org/10.2514/1.I010796.

- [30] Nielsen, E. J., and Anderson, W. K., "Aerodynamic design optimization on unstructured meshes using the Navier-Stokes equations," AIAA Journal, Vol. 37, No. 11, 1999. https://doi.org/10.2514/2.640, publisher: AMERICAN INST OF AERONAUTICS AND ASTRONAUTICS.
- [31] Nielsen, E. J., Lu, J., Park, M. A., and Darmofal, D. L., "An implicit, exact dual adjoint solution method for turbulent flows on unstructured grids," *Computers and Fluids*, Vol. 33, No. 9, 2004, pp. 1131–1155. https://doi.org/10.1016/j.compfluid.2003.09. 005, iSBN: 1757864881.
- [32] Jasa, J. P., Hwang, J. T., and Martins, J. R. R. A., "Open-source coupled aerostructural optimization using Python," *Structural and Multidisciplinary Optimization*, Vol. 57, No. 4, 2018, pp. 1815–1827. https://doi.org/10.1007/s00158-018-1912-8, publisher: Springer.
- [33] Secco, N. R., Kenway, G. K. W., He, P., Mader, C. A., and Martins, J. R. R. A., "Efficient mesh generation and deformation for aerodynamic shape optimization," AIAA Journal, Vol. 59, No. 4, 2021, pp. 1151–1168. https://doi.org/10.2514/1.J059491.
- [34] "FUNtoFEM code,", 2022. URL https://github.com/smdogroup/funtofem.
- [35] "DAFoam documentation,", 2022. URL https://dafoam.github.io.
- [36] Balay, S., Buschelman, K., Gropp, W. D., Kaushik, D., Knepley, M. G., McInnes, L. C., Smith, B. F., and Zhang, H., "PETSc Web page,", 2009.
- [37] Martins, J. R. R. A., and Hwang, J. T., "Review and unification of methods for computing derivatives of multidisciplinary computational models," *AIAA Journal*, Vol. 51, No. 11, 2013, pp. 2582–2599. https://doi.org/10.2514/1.J052184.
- [38] Gill, P. E., Murray, W., and Saunders, M. A., "SNOPT: An SQP algorithm for large-scale constrained optimization," *SIAM Review*, Vol. 47, No. 1, 2005, pp. 99–131. https://doi.org/10.1137/S0036144504446096, publisher: SIAM.
- [39] Kenway, G. K. W., Kennedy, G. J., and Martins, J. R. R. A., "A CAD-Free approach to high-fidelity aerostructural optimization," *Proceedings of the 13th AIAA/ISSMO multidisciplinary analysis optimization conference*, Fort Worth, TX, 2010. https://doi.org/10.2514/6.2010-9231.
- [40] Casalino, D., Grande, E., Romani, G., Ragni, D., and Avallone, F., "Definition of a benchmark for low Reynolds number propeller aeroacoustics," *Aerospace Science and Technology*, Vol. 113, 2021, p. 106707.
- [41] Pettingill, N. A., Zawodny, N. S., Thurman, C., and Lopes, L. V., "Acoustic and performance characteristics of an ideally twisted rotor in hover," *AIAA Scitech 2021 Forum*, 2021, p. 1928.